High-resolution 3-D P-wave velocity model for the East Ventura - San Fernando basin, California, and relocation of events in the Northridge and San Fernando aftershock sequences

Jose Pujol
Department of Earth Sciences
The University of Memphis
Memphis, TN 38152, USA

Karl Mueller
Department of Geological Sciences
University of Colorado
Boulder, CO 80309, USA

Peng Shen
TOTAL E&P USA
800 Gessner, Suite 700
Houston TX, 77024

Vani Chitupolu
Formerly: Department of Computer Science
The University of Memphis
Memphis, TN 38152, USA

Abstract

We determined a high-resolution 3-D P-wave velocity model for an 80 km x 80 km area around the San Fernando valley using events recorded from 1981 to 2000 as well as 799 aftershocks of the 1971 San Fernando earthquake recorded by a portable network. The total number of events and stations used were 13,455 and 101. Most of the events are aftershocks of the 1994 Northridge earthquake. The inversion software includes a ray tracing subroutine designed to handle the sharp lateral velocity variations that exist in the area. The resulting model shows an overall good agreement with the Southern California Earthquake Center (SCEC) 3-D velocity model, but images the deeper structure of the San Fernando valley in more detail. In addition, our results are supported by the remarkable agreement with a density model derived from gravity data along a 55 km long profile. An approximately 10 km wide and sharply-defined zone of Northridge aftershocks occurred in basement rocks between about 8 and 20 km depth and define the fault that slipped during the mainshock. Horizontal slices at deep (8-18 km) levels show that the Northridge earthquake occurred within a high-velocity basement block that may have controlled the size of the earthquake. The fault plane inferred from the seismicity is in good agreement with the geodetic fault plane determined by Hudnut et al. (1996) assuming uniform slip. Most of the aftershocks of the Northridge earthquake occurred within the sedimentary rocks of the San Fernando basin, with a large concentration of events located to the east of the eastern boundary of the mainshock fault plane. The latter events form a zone that dips about 45° to the southwest at depths less than about 14 km that may represent a lateral ramp. This zone terminates at the steeply inclined eastern edge of the San Fernando basin. These events do not lie on the mainshock fault plane, and because the San Fernando aftershocks also lie east of the Northridge fault plane, the San Fernando and the Northridge mainshocks occurred on en-echelon conjugate faults (i.e., they do not abut each other). In addition, an 8 km wide cross section along the density model referred to above suggests the Northridge aftershocks east of the mainshock and most of the aftershocks of the San Fernando earthquake illuminate two thrust faults that contain the same high-velocity basement block in their footwalls. The velocity model produced by our analysis suggests thrust faults formed by modern contraction in this region are strongly influenced by prior basin and basement block geometry.

Introduction

The M = 6.7 Northridge, California, earthquake occurred on a previously unknown blind thrust fault in 1994 and more than ten years later a number of important questions still remain partially or totally unanswered. Chief among these is the exact nature of the 3-D velocity variations in the area and its relation to the mainshock rupture and aftershocks distribution. Existing velocity models (e.g., Hauksson and Haase, 1997; Mori et al. 1995; Pujol, 1996; Zhao and Kanamori, 1995) have relatively low resolution, which limits their usefulness for detailed studies of deep basin and basement structure. The lack of a detailed 3-D velocity model has important implications in the context of seismic hazard studies. As is well known, the amplitude of the ground motion caused by an earthquake increases with the thickness of sedimentary basin fill. For example, Wald and Graves (1998) found that in the San Fernando and Los Angeles basins the ground motion can be amplified by factors of about three and four with respect to rock sites, and that the 3-D velocity models existing at that time were inadequate to generate synthetic waveforms showing this amplification. The need for more accurate models has been addressed, in part, by Magistrale et al. (2000), who developed the Southern California Earthquake Center (SCEC) 3-D velocity model, which covers the major basins in southern California. The model is

based on an empirical relation between the maximum depth of burial of sediments and their P wave velocity and age (Faust's law), and on empirical relations involving P wave velocity, density and Poisson ratio, which are used to estimate S wave velocities. P and S wave velocities for the shallower depths (< 300 m) were determined using borehole data. One of the parameters in Faust's law was calibrated using borehole information. For the San Fernando basins four boreholes were available, the deepest reaching about only 3.5 km depth, so that for larger depths the velocity model has not been calibrated. For rocks outside of the basins the SCEC model uses the 3-D velocity model of Hauksson (2000). This model has been computed for a 15 km x 15 km horizontal grid at depths of 1, 4, 6, 10, 15, 17 and km.

More recently, Süss and Shaw (2003) derived a high-resolution 3-D velocity model for the Los Angeles basin based on more than 7000 stacking velocities derived from reflection seismology data. The model was calibrated using more than 150 sonic logs. Süss and Shaw compared the sonic and SCEC velocities and found that the standard deviation of the velocity differences is about 440 m/s, which represents about 20% of the model velocities. A similar result was obtained when comparing the Süss and Shaw and SCEC models, and, in addition, it was observed that the SCEC model generally underestimates the velocities near the center of the basin and overestimates them near the border. These results are consistent with those of Stewart et al. (2005), who found that the SCEC velocities are too high in the shallow parts of the basin and too low in the deeper parts. According to Süss and Shaw (2003), the difference between their model and the SCEC model is due to Magistrale et al.'s (2000) use of a 1-D function to represent the velocities within a given stratigraphic interval, which ignores lateral velocity gradients due to facies variations within stratigraphic intervals across the basin. This means that the pattern detected by Süss and Shaw (2003) may affect the rest of the SCEC model, not just the Los Angeles basin.

Although the SCEC model represents a major step towards a realistic 3-D velocity model for the southern California basins, it would be desirable to determine its validity where it has not been calibrated with borehole information and to include a higher resolution model for the basement rocks that underlie the sedimentary basins. One of the goals of the research described here is to provide this additional information. The main difference between our results and previously published models is the high resolution of our 3-D velocity model, which was possible because of the use of inversion software that includes exact ray tracing software designed to handle sharp lateral velocity variations. The reliability of our model is attested by the overall similarity to the SCEC model in the sedimentary fill, and the remarkable agreement with a density model derived from gravity data (Langenheim et al., 2000) along a 55 km long profile.

Data and inversion method

We used P-wave first arrivals from 12,656 events recorded during 1981-2000 by 81 stations from the Southern California Seismic Network and from a portable network deployed to record aftershocks of the Northridge earthquake (Edelman et al., 1994). In addition, we used 799 aftershocks of the 1971 San Fernando earthquake recorded by a portable network of 20 stations (Wesson et al., 1971). The epicenters of these events and the locations of the station used are shown in Fig. 1. The total number of arrivals was 192,421. These events were selected under the criteria that they had largest azimuthal gap ≤ 150° and rms residual ≤ 0.5 s when located with a single event-location program that uses quality weights only and the standard 1-D model based

on the results of Hadley and Kanamori (1977). This model has three layers with thicknesses of 5.5, 10.5 and 16 km, respectively, and respective velocities of 5.5, 6.3, and 6.7 km/s. A number of portable stations that recorded Northridge aftershocks were not used because of timing errors. The second largest aftershock (M = 5.6) occurred 11 hours after the mainshock and was included in the dataset in spite of a gap of 164°. Unfortunately, the arrival times for the M = 5.9 aftershock, which followed the mainshock by one minute, are affected by considerable error and could not be used in the inversion, and the location used here comes from the SCEC catalog.

For the velocity determination we used the 3-D tomographic inversion package developed by H. Benz (Benz et al., 1996), which incorporates the software of Podvin and Lecomte (1991) for the computation of travel times. A unique feature of this software is its ability to handle sharp velocity variations accurately. This package was recently applied to P and S wave arrival times from Taiwan earthquakes, and the resulting velocity images have unprecedented resolution (Kim, 2003; Kim et al., 2005). In Benz's package the earthquake location and velocity determination problems are decoupled using the method of separation of parameters (Pavlis and Booker, 1983). As traveltime is a linear function of slowness (i.e., the reciprocal of velocity), this is the parameter that is actually inverted for. The inversion process is iterative; after each iteration the 3-D slowness model is updated and the events are relocated with the new model. The magnitude of the slowness adjustments is controlled by the constraint that the Laplacian of the slowness field must vanish. The corresponding equation is multiplied by a weighting factor, whose value is allowed to change as the iterations proceed. To assure a smooth inversion process the number of iterations was ten, with the Laplacian weight relatively large (64) for the earlier iterations and smaller (20) for the last ones, with an intermediate value in between. The velocity model is parameterized into blocks of equal size. In our analysis the study area is 80 km by 80 km and the blocks are cubes with sides 2 km long. The travel times were computed using blocks with sides 1 km long. Because the elevations can be as high as 1.6 km for stations in the San Gabriel mountains, all the computations are referred to a baseline reference of -2 km. This baseline constitutes the origin of the depth coordinate system. This is why the subsequent figures showing velocity depth cross sections do not start at zero depth. The event depths, however, are referenced to sea level.

Results

The results reported here use as an initial model velocity the 1-D model derived by Hauksson et al. (1995) with the following modification. The first layer was divided into two 2-km thick layers, the upper one with a velocity of 4.5 km/s and the lower one with the original velocity (4.8 km/s) (see Table 1). The initial event locations, however, where determined using the standard 1-D model described above. The combined rms residual for all the events in the first and last (tenth) iteration was 0.17 s and 0.07 s. The epicenters of the relocated events are shown in Fig. 1 and most of the hypocenters in Fig. 2. The difference between the initial and inversion event locations is quasi-systematic. On average, the initial locations are 1.0 km to the east and 0.5 km to the south of the inversion locations, and 1.5 km deeper. The epicentral differences observed are in agreement with earlier results of Pujol (1996) and are due to the presence of the large lateral velocity variations in the area (see below). In addition to these systematic variations, the initial locations show larger scatter than the inversion locations, with the average value of the epicentral differences equal to 1.5 km. We also run the inversion with two initial velocity models similar to the previous one with the velocity in the upper layer changed to 3.5 and 4.0 km/s. The effect of these changes on the inversion results is minor. The major features of the

corresponding velocity models, discussed below, do not change; the most important differences are in their shallower parts. In addition, the inversion of realistic synthetic arrival time data generated using 3-D velocity models for the Northridge area determined using different data subsets show that the observed velocity variations are not an artifact of the inversion method.

The most compelling support for the validity of our model comes, however, from comparison with the SCEC 3-D velocity model and with a density model derived from the analysis of gravity data. We consider the SCEC model first, which was sampled at the centers of the blocks of our model, with the first depth at 1 km. The SCEC model, however, has the surface as zero depth, and because the station elevations range between about 0 and 1.6 km in our study area, a direct comparison with our model is not strictly possible. For example, the station elevations range between about 0 and 1.2 km within the boxes A-F in Fig. 1 and between 0 and 0.7 km within the box labeled **a**. For this reason, for the SCEC model we used a base elevation of -0.6 km. Figures 2 and 3 show velocity cross sections for blocks A-F for the inversion and SCEC velocity models. Comparison of the two figures shows that our model has an overall good agreement with the SCEC model, although there are some differences. For example, our model resolves more detail of the geometry of the San Fernando basin (e.g., in cross sections E and F) than is predicted by the SCEC model. On the other hand, the SCEC model contains high velocity layers between about 5 and 8 km depth in cross sections A-C that do no appear in our model.

A N-S oriented 55-km long density model derived by Langenheim et al. (2000) from the analysis of gravity data also supports our results. As shown in Fig. 4, the agreement between the velocity and density models is surprisingly good. For a comparison, Fig. 4 also shows the initial velocity model and the SCEC model. Note that the SCEC model does not match the density model as well as our results and in particular it does not define blocks of apparently overthrust high-velocity rocks that are exposed in the nearby San Gabriel mountains. For another comparison, the velocities in the model of Hauksson and Haase (1997) are shown in Fig. 5. This model has a 10 km x 10 km horizontal grid at depths of 1, 4, 6, 8, 12, 16 and 20 km and also does not resolve the velocity variations in the San Fernando basin, in addition to being affected by possible artifacts.

Discussion

Before discussing our results we must consider the depth of basement rocks in the region. As no borehole penetrates the basement-cover contact in the deeper parts of the East Ventura - San Fernando basin we relied on information derived by Lutter et al. (2004) from analysis of the LARSE II transect, which crosses basement outcrops in the Santa Monica Mountains and the southern part of the central Transverse Ranges. For these two areas the basement velocity (beneath weathered layers) is between 5.75 and 6.0 km/s and between 5.5 and 6.0 km/s, respectively. In the velocity cross sections shown in Figs. 2-4 the 6 km/s contour line coincides with the boundary between the yellow and reddish areas and will be used to approximate the floor of the basin, or basement-cover contact. This allows us to consider the relation between seismicity and basin structure as constrained by the velocity model. Unless otherwise stated, the cross sections referred to below are those shown in Fig. 2.

A clear result of our inversion is that most of the Northridge earthquake aftershocks occurred within the basin. The seismicity in basement rocks is concentrated in cross sections D and E,

with the events located along clear lineations that define the fault that slipped during the mainshock. Note, however, that most of the events form clusters, which are even tighter when considering the events that occurred only in 1994 (Fig. 3). The strong cluster in cross section D centered at about 9 km depth marks the intersection of the mainshock rupture plane with the bottom of the basin. Langenheim et al. (2000) inferred this result from their analysis of gravity data, while Hauksson et al. (1995) explained the cluster in terms of deformation of an overlying anticlinal fold.

Another important result is that the large concentration of aftershocks to the east of the green line in Fig. 1 did not occur on the fault plane that contained the mainshock, as suggested by Pujol (1996). As cross section F shows, most of the events are shallower than about 14 km and form a wide band of seismicity located mostly within the sediments of the San Fernando basin and near its eastern edge. Interestingly, the location of the largest Northridge aftershock, which occurred one minute after the mainshock, is in the vicinity of these events. Therefore, it can be argued that this aftershock produced stress changes at the end of the mainshock rupture that triggered the seismicity seen here. Unfortunately, the location of this aftershock is not well determined and the focal mechanism is not available (Dreger, 1997; Hauksson et al., 1995), which prevents testing of this hypothesis.

The events in the center of cross section B between about 8 and 15 km depth can be interpreted as corresponding to the northeast dipping Santa Susana fault (Pujol, 1996; Yeats, 2001). When only the aftershocks recorded in 1994 are plotted, the fault appears as a much narrower feature (Fig. 3). The second largest aftershock of the Northridge earthquake is aligned with this feature. It is not clear, however, whether its depth is reliable given that its initial largest azimuthal gap was rather large (164°). For this event, our location, the catalog location, and the locations determined by Hauksson et al. (2003) and Shearer et al. (2003) (see below) are all different.

The widespread distribution of aftershocks in the basin raises the question of what triggers them. This question has already been addressed by other researchers, but the answer is inconclusive. Hardebeck et al. (1998) showed that a model based on static stress changes could not explain the first month of Northridge aftershock sequence better than it could explain a random distribution of aftershocks. However, the model seems to be appropriate for the aftershocks of the 1992 Landers earthquake. Hardebeck et al. (1998) noted that this difference may be due to differences in fault strength and that the model may need to incorporate this parameter as well as tectonic regime and regional stress levels. It is also possible that the standard assumption of dislocation in a half-space used to compute changes in the stress tensor is not appropriate in areas with geometries as complex as that in the San Fernando basin. More recently, Gavrilenko (2005) investigated the possibility that the aftershocks that follow large earthquakes may be related to the fluids that circulate in the crust after their occurrences (Muir-Wood and King, 1993). The Northridge earthquake was accompanied by clear hydrologic effects. For example, a creek about 55 km to the WNW of the epicenter had a coseismic discharge increase of 40% and a new oil seep began to flow in the northern Ojai Valley (Sneed et al., 2003, and references therein). Gavrilenko (2005) modeled the fluid redistribution that follows a large earthquake using the equations of poroelasticity and related his results to changes in the Coulomb failure function. Application of this approach to the Northridge earthquake shows a good agreement between the observed and predicted time dependence of the aftershocks, although their spatial distribution was not well recovered, particularly for the events

below about 8.5 km. As this is approximately the depth of the basin in cross sections D and E in Fig. 2, this result also points out to the need for an earth model that incorporates realistic variations in physical properties. In contrast, Bosl and Nur (2002) successfully modeled the timing and location of the Landers aftershocks using an approach similar to that of Gavrilenko (2005).

The fact that the Northridge aftershocks in cross section F did not occur within the mainshock fault plane has important implications in the context of the relation between the Northridge and the San Fernando earthquakes. The latter and most of its recorded aftershocks have epicenters east of the green line in Fig. 1 and hypocenters in cross section E, underneath a sheet of overthrust basement rocks. When the aftershocks in cross sections E and F are plotted together (Fig. 6) the San Fernando fault appears to truncate the Northridge fault, as Mori et al. (1995) suggested, but this interpretation is not correct because the Northridge rupture is represented by the events in cross sections D and E. Therefore, the Northridge and the San Fernando faults do not abut each other; they actually constitute en-echelon conjugate reverse faults.

Additional insight into the relation between velocity structure and seismicity can be inferred by examination of horizontal slices (Fig. 7), which confirm that most of the Northridge aftershocks down to a depth of about 10 km occurred within sedimentary rocks of the basin. Therefore, it can be argued that the distribution of aftershocks was controlled by the nature of the mainshock rupture, by the distribution of the sediments and by the faults within it. In the 8-10 km slice we also see the cluster of events that marks the intersection of the bottom of the basin with the Northridge fault plane and the cluster of events to the east of that plane. As depth increases, the number of events in the basement decreases, and below about 14 km most of them occur only in the vicinity of the fault plane. The horizontal slices also show that at about 8-10 km depth a high-velocity area (indicated by the arrow) begins to emerge to the south of, and adjacent to, the fault plane. As the depth increases, this area becomes elongated in a northeast direction and intersects the fault plane. This observation is important because it can be interpreted as an indication that the size of the Northridge fault is controlled by the width (about 10 km) and depth extent of a high-velocity rock body. The relation between high-velocity rocks and the rupture zone of large earthquakes, including the Northridge earthquake, is not new (Zhao and Kanamori, 1995, and references therein). What is new in our work is the high resolution of the velocity model, which allows identification of the asperity that broke during the mainshock.

We next consider the implications of these observations in the context of the rupture models for the Northridge earthquake determined using geodetic data alone and a combination of geodetic and seismic data, which show significant differences. The fault plane shown in Figs. 1 and 7 corresponds to the geodetic fault plane determined by Hudnut et al. (1996) under the assumption of uniform slip. Assuming variable slip over a larger fault area, these authors found a large-slip patch to the northwest and updip of the hypocenter, with slip less than 1 m above 5 km depth. The geodetic models represent the co-seismic effect of the mainshock plus the contribution of two large aftershocks that occurred shortly after the mainshock (having magnitudes of 5.9 and 5.6). The uniform-slip geodetic fault plane corresponds to the area of largest slip and is in excellent qualitative agreement with the fault plane that we infer from the distribution of basement seismicity and with the presence of the band of high velocity rocks below 8 to 10 km. Wald et al. (1966) used geodetic and strong-ground motion and teleseismic data separately and in combination, and found that the slip model based on geodetic data alone is much smoother than the model based on seismic data and that the geodetic model does not

correctly predict the observed seismic ground motion. Two points must be noted here. First, the fault geometry was assumed at the outset, with the fault plane covering the whole epicentral area, which includes eastern events that were not along the fault plane, as discussed earlier. Second, the disagreement between the synthetic seismic data computed using the geodetic slip model and the observed data should not be surprising, as the computations were carried out for a layered velocity model, which is an oversimplification in view of the large lateral velocity variations that exist in the area. These variations should have a significant effect on the observed seismic data, and ignoring them when computing slip will probably translate into a slip model more complicated than that derived from geodetic data.

Our results also bear on the question of the deformation style in the San Fernando basin. Huftile and Yeats (1996) and Yeats and Huftile (1995) argued for thick-skinned shortening, while Davis and Namson (1994) modeled the region as deforming in a thin-skinned fashion with large flat segments and active thrusts. Carena and Suppe's (2002) work favored a mix of styles, with basement-involved shortening at deep levels and more thin-skinned strain occurring at shallower levels (e.g., Northridge and San Fernando thrusts vs. Santa Susana thrust). Our work strongly supports the thick-skinned model for the Northridge and San Fernando earthquakes, without evidence for the horizontal detachment proposed by Davis and Namson (1994), and also suggests that inversion tectonics plays an important role in shortening in the San Fernando region. The evidence in favor of inversion is twofold. First we note the presence of a high-velocity basement block imaged in the footwall of the San Fernando thrust. Second, there is a lack of apparent thrust offset in the Northridge fault across the well-imaged floor of the San Fernando basin, which appears to even have normal-sense displacement in cross sections C, D, and F in Fig. 2. These facts thus support the concept that the Northridge thrust may be a reactivated normal fault that is currently accommodating crustal shortening. This is consistent with the known history of the Los Angeles basin and environs, where a record of Miocene extension is well documented.

Finally, we compare our locations to those determined by Hauksson et al. (2003) using a double-difference method, and by Shearer et al. (2003) using source-specific station terms and cluster analysis. The locations are available from the Southern California Earthquake Data Center and the data analyses are described in Hauksson and Shearer (2005) and Shearer et al. (2005). Figures 8 and 9 and 10 and 11 show the Hauksson et al. (2003) and Shearer et al. (2003) locations, respectively, for the events in Figs. 1 and 2 recorded between 1984 and 2000. The three sets of locations are clearly different, with the Hauksson et al. (2003) locations much more scattered than the other two sets of locations. Hauksson et al. (2003) and Shearer et al. (2003) relocated over 300,000 events in southern California, and although no attempt was made to optimize the parameters used in the location processes, the differences in clustering are significant, which points to possible intrinsic differences in the methods used and their performance when the events are in areas of large velocity variations, such as those that exist in our study area. Although double-difference methods are assumed to improve relative locations even in the presence of velocity variations, this assumption has not been validated. On the contrary, Michelini and Lomax (2004) showed with realistic synthetic data that the double-difference method can produce locations affected by significant errors when incorrect velocity models are used. The source-specific station terms method, on the other hand, attempts to account for 3-D velocity variations. Station terms are station corrections terms similar to those used in the joint hypocentral determination method (JHD), and although the use of these corrections account for some of the effects of lateral velocity variations, thus improving relative

locations, it cannot be assumed that the absolute locations will be recovered well. Whether this happens or not is problem dependent (Pujol, 2000). In the particular case of the east Ventura – San Fernando basin it was shown (Pujol, 1996) that the absolute JHD locations are affected by a quasi-systematic epicentral shift to the northwest of about 2.7 km, while the single event locations are shifted about 2 km to the southeast. Compared to our locations, those of Shearer et al. (2003) show systematic differences. In general, their epicenters are somewhat to the east of ours, the events identified by the arrow in box F of Fig. 1 form a longer distribution, and all the events are consistently deeper (2.4 km on average). Unless the Shearer et al. (2003) method is tested with realistic synthetic data it will not be possible to assess the effect of the 3-D velocity variations on their event locations.

Conclusions

The high-resolution 3-D velocity model presented here allows imaging of the deep structure of the East Ventura – San Fernando basin in great detail. This, in turn, allows studying the relation between basin structure and seismicity. The most important observations are the following.

1. The fault that ruptured during the Northridge mainshock occurred within a high-velocity basement block about 10 km wide that may have controlled the size of the earthquake. The fault plane inferred from the seismicity is in good agreement with that derived from the inversion of geodetic data.

2. Most of the Northridge aftershocks occurred within the sedimentary rocks of the basin. The mechanism that triggered them remains enigmatic.

3. The San Fernando earthquake and most of its recorded aftershocks are to the east of the eastern boundary of the Northridge mainshock fault plane, which means that the two earthquakes occurred on en-echelon faults (i.e., they do not abut each other).

4. A large number of Northridge aftershocks also occurred to the east of the mainshock fault plane. These events and the San Fernando aftershocks illuminate two thrust faults that abut each other and have the same high-velocity block in their footwalls.

5. The northeast-dipping Santa Susana fault was active during the Northridge sequence.

6. Our results strongly support a thick-skinned deformation style for the basin and suggest that inversion tectonics plays an important role in the shortening in this region.

Acknowledgments. We thank Dr. H. Benz for permission to use his tomographic inversion package and Dr. G. Fuis for providing the San Fernando aftershock data. The rest of the data were provided by the Southern California Earthquake Center. This work was funded by NEHRP grant 03HQGR0064. The conclusions presented here should not be interpreted as representing the opinion of the U.S.G.S.

References

Benz, H., B. Chouet, P. Dawson, J. Lahr, R. Page, and J. Hole (1996). Three-dimensional P and S wave velocity structure of Redoubt volcano, Alaska, *J. Geophys. Res*. **101**, 8111-8128.

Bosl ,W. and A. Nur (2002). Aftershocks and pore fluid diffusion following the 1992 Landers earthquake, J. Geophys. Res. **107** doi:10.1029/2001JB000155.

Carena, S. and J. Suppe (2002). Three-dimensional imaging of active structures using earthquake aftershocks: the Northridge thrust, California. *J. Struct. Geol*. **24**, 887-904.

Davis, T and J. Namson (1994). A balanced cross-section of the 1994 Northridge earthquake, Southern California, *Nature* **372**, 167-169.

Dreger, D. (1997). The large aftershocks of the Northridge earthquake and their relationship to mainshock slip and fault-zone complexity, *Bull. Seism. Soc. Am*. **87**, 1259-1266.

Edelman, A., and 15 others (1994). Portable instrument data set from the January 17, 1994 earthquake aftershock sequence, *Eos Trans*. *AGU* **75**, (44), Fall Meeting Suppl., F457.

Gavrilenko, P. (2005). Hydromechanical coupling in response to earthquakes: on the possible consequences for aftershocks. *Geophys. J. Int*. **161**, 113-129.

Hadley, D. and H. Kanamori (1977). Seismic structures of the Transverse Ranges, California, *Geol. Soc. America Bull.* **88**, 1469-1478.

Hardebeck, J., J. Nazareth, and E. Hauksson (1998). The static stress change triggering model: Constraints from two southern California aftershock sequences, *J. Geophys. Res*. **103**, 24,427-24,437.

Hauksson, E. (2000). Crustal structure and seismicity distribution adjacent to the Pacific and North America plate boundary in southern California, *J. Geophys. Res*. **105**, 13,875-13,903.

Hauksson, E., W-C. Chi, and P. Shearer (2003). Comprehensive waveform cross-correlation of southern California seismograms: Part 1. Refined hypocenters obtained using the double-difference method and tectonic implications (abstract), *Eos Trans*. *AGU* **84** (46), Fall Meet. Suppl., Abstract S21D-0325.

Hauksson, E., and J. Haase (1997). Three dimensional Vp and Vp/Vs velocity models of the Los Angeles basin and central Transverse Ranges, California, *J. Geophys. Res*. **102**, 5423-5453.

Hauksson, E., L. Jones, and K. Hutton (1995). The 1994 Northridge earthquake sequence in California: seismological and tectonic aspects, *J. Geophys. Res.* **100**, 12,335-12,555.

Hauksson E. and P. Shearer (2005). Southern California hypocenter relocation with waveform cross-correlation, Part 1: results using the double-difference method, *Bull. Seism. Soc. Am*. **95**, 896-903.

Hudnut, K., and ten others (1996). Co-seismic displacements of the 1994 Northridge, California, earthquake, *Bull. Seism. Soc. Am*. **86**, S19-S36.

Hufttile, G., and R. Yeats (1996). Deformation rates across the Placerita (Northridge Mw = 6.7 aftershock zone) and Hopper Canyon segment of the western Transverse Ranges deformation belt, *Bull. Seism. Soc. Am*. **86**, S3-S18.

Kim, K. (2003). Subsurface structure, seismicity patterns, and their implications to tectonic evolution in Taiwan, Ph.D. dissertation, The University of Memphis.

Kim, K.-H., Chiu, J.-M., J. Pujol, K.-C. Chen, B.-S. Huang, Y.-H. Yeh, and P. Shen (2005). Three-dimensional Vp and Vs structural models associated with the active subduction and collision tectonics in the Taiwan region, *Geophys. J. Int.* **162,** 204–220.

Langenheim, V., A. Griscom, R. Jachens, and T. Hildenbrand (2000). Preliminary potential-field constraints on the geometry of the San Fernando basin, southern California, U. S. Geol. Survey Open-file Report 00-219.

Lutter, W. and 15 others (2004).Upper crustal structure from the Santa Monica mountains to the Sierra Nevada, southern California: tomographic results from the Los Angeles Regional Seismic Experiment, Phase II (LARSE II), *Bull. Seism. Soc. Am.* **94**, 619-632

Magistrale, H., S. Day, R. Clayton, and R. Graves (2000). The SCEC southern California reference three-dimensional seismic velocity model version 2, *Bull. Seism. Soc. Am.* **90**, S65-S76.

Michelini, A. and A. Lomax (2004). Effect of velocity structure errors on double-difference earthquake location, *Geophys. Res. Lett*., doi:10.1029/2004GL019682.

Mori, J., D. Wald, and R. Wesson (1995). Overlapping fault planes of the 1971 San Fernando and 1994, California earthquakes, *Geophys. Res. Lett*. **22**, 1033-1036.

Muir-Wood, R. and G. King (1993). Hydrological signatures of earthquake strain, *J. Geophys. Res*. **98**, 22,035-22,068.

Pavlis, G. and J. Booker (1983). Progressive multiple event location (PMEL), *Bull. Seism. Soc. Am.* **73**, 1753-1777.

Podvin, P., and I. Lecomte (1991). Finite difference computation of traveltimes in very contrasted velocity models: A massively parallel approach and its associated tools, *Geophys. J. Int*. **105**, 271-284.

Pujol, J. (1996). An integrated 3D velocity inversion -- joint hypocentral determination relocation analysis of events in the Northridge area, *Bull. Seism. Soc. Am*. **86**, S138-155.

Pujol, J. (2002). Joint event location - The JHD technique and applications to data from local seismic networks. In: Advances in seismic event location, Thurber, C., and N. Rabinowitz, Eds. Kluwer Academic Publishers, 163-204.

Shearer, P., E. Hauksson, and G. Lin (2005). Southern California hypocenter relocation with waveform cross-correlation, Part 2: results using source-specific station terms and cluster analysis, *Bull. Seism. Soc. Am.* **95**, 904-915.

Shearer, P., E. Hauksson, G. Lin and D. Kilb (2003). Comprehensive waveform cross-correlation of southern California seismograms: Part 2. Event locations obtained using cluster analysis *Eos Trans. AGU* **84** (46), Fall Meet. Suppl., Abstract S21D-0326.

Sneed, M., D. Galloway, and W. Cunningham (2003). Earthquakes—Rattling the Earth's Plumbing System, U.S. Geological Survey Fact Sheet 096-03 (***http://pubs.usgs.gov/fs/fs-096-03/***).

Stewart, J., Y. Choi, R. Graves, and J. Shaw (2005). Uncertainty of southern California basin depth parameters, *Bull. Seism. Soc. Am*. **95**, 1988-1993.

Süss, M. and J. Shaw (2003). P wave seismic velocity structure derived from sonic logs and industry reflection data in the Los Angeles basin, California, *J. Geophys. Res*. **108,** doi:10.1029/2001JB001628

Wald, D., T. Heaton, and K. Hudnut (1996). The slip history of the 1994, Northridge, California, Earthquake determined from strong-motion, teleseismic, GPS and leveling data, *Bull. Seism. Soc. Am*. **86**, S49-S70.

Wald, D. and R. Graves (1998). The seismic response of the Los Angeles basin, California, *Bull. Seism. Soc. Am*. **88**, 337-356.

Wesson, R., W. Lee, and J. Gibbs (1971). Aftershocks of the earthquake. In: The San Fernando, California, earthquake of February 9, 1971, U. S. Geol. Survey Professional Paper 733.

Yeats, R. (2001). Neogene tectonics of the east Ventura and San Fernando basins, California: an overview, in: Wright, T. and R. Yeats (eds.), Geology and Tectonics of the San Fernando Valley and east Ventura basin, California, Pacific Section, American Association of Petroleum Geologists, Guidebook GB 77, 9-36.

Yeats, R. and G. Huftile (1995). The Oak Ridge fault system and the 1994 Northridge earthquake, *Nature* **373**, 418-420.

Zhao, D and H. Kanamori (1995). The 1994 Northridge earthquake: 3-D crustal structure in the rupture zone and its relation to the aftershock location mechanisms, *Geophys. Res. Lett*. **22**, 763-766.

Table 1
Initial 1-D velocity model for the tomographic inversion

Depth to top of layer (km)	P-wave velocity (km/s)
0	4.50
2	4.80
4	5.78
6	6.15
8	6.30
12	6.44
16	6.54
20	6.72
32	7.76

FIGURE CAPTIONS

Fig. 1. Area for which a 3-D velocity model has been determined. Blue dots indicate the epicenters of 12647 seismic events recorded between 1981 and 2000 by 81 permanent and portable stations (magenta open circles). Most of the events within the blue boxes are aftershocks of the 1994 Northridge earthquake. Red dots indicate epicenters of 799 aftershocks of the 1971 San Fernando earthquake recorded during February-April 1971 by 20 portable stations (magenta crossed circles). The centers of the large black and red circles indicate the epicenters of the Northridge mainshock and its largest aftershocks, which occurred one minute (M = 5.9, box F) and about 11 hours (M = 5.6, box B) later. The epicenter of the San Fernando earthquake is indicated by the green circle. The locations of the largest aftershock and the San Fernando mainshock are from the U.S. Geological Survey and Southern California Earthquake Data Center. The location of the M = 5.9 event is not well constrained. The locations of all the other events were determined as part of the velocity inversion - earthquake relocation process. Black lines indicate faults. The San Andreas and San Gabriel faults are labeled SAF and SGF. The bold box is the projection of the Northridge earthquake fault plane determined by Hudnut et al. (1996) using geodetic data and assuming uniform slip. The events in the boxes A through H and in the box labeled **a** are shown in cross section form in Figs. 2 and 6. Most of the San Fernando events are to the east of the green dashed line while the Northridge main shock rupture occurred to the west of that line. The prominent band of Northridge seismicity in a roughly N-S direction (identified by the red arrow in box F) did not occur within the area that ruptured during the main shock. The events and velocity within box **a** are shown in cross section form in Figs. 4-6.

Fig. 2. Depth cross sections for the 3-D velocity model determined by inversion and the events in the boxes A through H in Fig. 1. The width of the cross sections is 5.3 km. The letters are on the southern ends of the cross sections. The velocities are assigned to the centers of the model blocks and are interpolated along planes passing through the centers of the cross sections. Black and magenta dots indicate Northridge and San Fernando aftershocks. The large circled asterisks in cross sections E, B and F indicate the Northridge mainshock, its two largest aftershocks and the San Fernando mainshock (see Fig. 1). The number in the right lower corner of each cross section denotes the number of events. Only the velocity blocks covered by a combined ray length of 0.1 km or more are shown. Note the correlation between seismicity and velocity. The events between about 10 and 20 km in D and E are within high-velocity, basement rocks, and form narrow and well-defined lineations. These events span about 10 km horizontally and basically define the width of the fault that slipped during the main shock. The Northridge aftershocks in F correspond mostly to those indicated by the red arrow in Fig. 1. Most of these events are shallower than about 14 km and form a band of seismicity within and near the edge of the basin. The north-dipping events in B below about 10 km probably occurred on the Santa Susana fault.

Fig. 3. Similar to Fig. 2 for the SCEC 3-D velocity model (Magistrale et al., 2000) and the events that occurred during 1994.

Fig. 4. Velocity depth cross section along the center of box **a** in Fig. 1 for three velocity models. Top: Initial velocity model. Center: Inversion model. All the blocks, regardless of the ray coverage, are shown. The polygons represent the bodies (simplified; see Fig. 5 for the original) used by Langenheim et al. (2000) to match a gravity profile. The red lines bound materials with densities ranging between 2.00 and 2.55 g/cc. The area bounded by red and green lines corresponds to low-density basement (2.65 g/cc). Elsewhere in the figure the density is 2.71 g/cc.

Note the excellent agreement between the extent of the low velocities in the Los Angeles (LAB), San Fernando (SFV) and Soledad (SB) basins and the low-density bodies, as well as the presence of high velocities in the areas of the Santa Monica (SMM) and the San Gabriel (SGM) mountains. Fig. 6 shows this cross section with a restricted ray coverage. Bottom: SCEC 3-D velocity model. This model does not fit the density model as well as the inversion model.

Fig. 5. Top: Similar to Fig. 4 for the 3-D velocity model of Hauksson and Haase (1997). The contour labels indicate velocities in km/s. The red arrows indicate possible artifacts in the model. Crosses indicate the locations of gravity stations. Bottom: Same as above including the gravity model. From Langenheim et al., 2000.

Fig. 6. Similar to Fig. 4 for the inversion velocity model for blocks having ray coverage of 0.1 km or larger. The fact that the initial model is one-dimensional indicates that the 3-D velocity variations seen in Fig. 4 for the blocks not shown here were determined in earlier iterations. Also shown are the events within box **a** in Fig. 1. The box width is 8 km. Note that the Northridge and San Fernando aftershocks are underlain by a wedge of basement, with the seismicity occurring where rocks with lower velocities are present.

Fig. 7. Map view of the inversion velocity model as a function of depth. The area covered is as in Fig. 1. Only blocks with ray coverage equal to 0.1 km or larger are shown. The numbers on the right upper corners indicate the depth range. Also shown are the epicenters of the relocated events. The numbers on the right lower corners indicate the number of events. The blue box corresponds to the geodetic fault plane in Fig. 1. The arrows point to a high velocity area below 8 km depth.

Fig. 8. Similar to Fig. 1. The events in that figure recorded between 1984 and 2000 are plotted here using the locations determined by Hauksson et al. (2003).

Fig. 9. Similar to Fig. 2. The events in that figure recorded between 1984 and 2000 are plotted here using the locations determined by Hauksson et al. (2003).

Fig. 10. Similar to Fig. 8 for the Shearer et al. (2003) event locations.

Fig. 11. Similar to Fig. 9 for the Shearer et al. (2003) event locations.

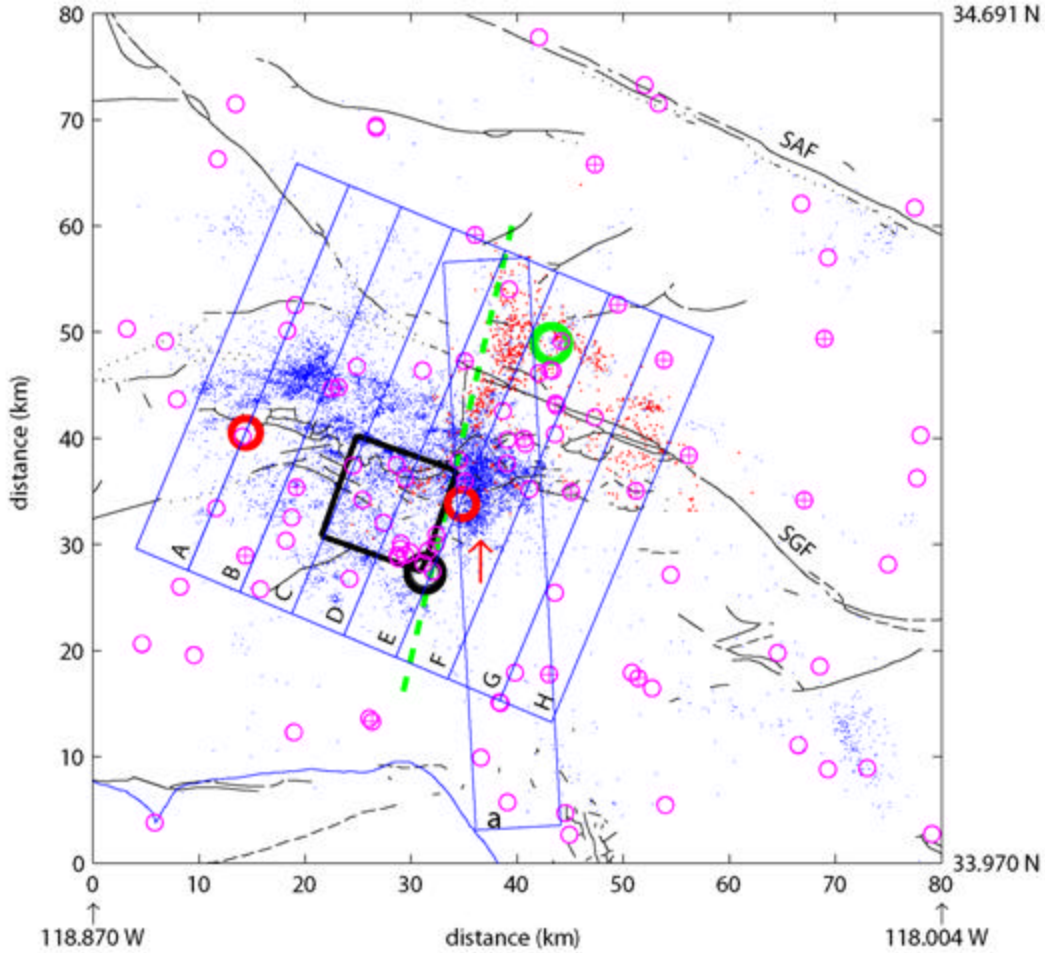
34.691 N
33.970 N
118.870 W
118.004 W
distance (km)
distance (km)
SAF
SGF
A
B
C
D
E
F
G
H
a
0
10
20
30
40
50
60
70
80

Figure 1

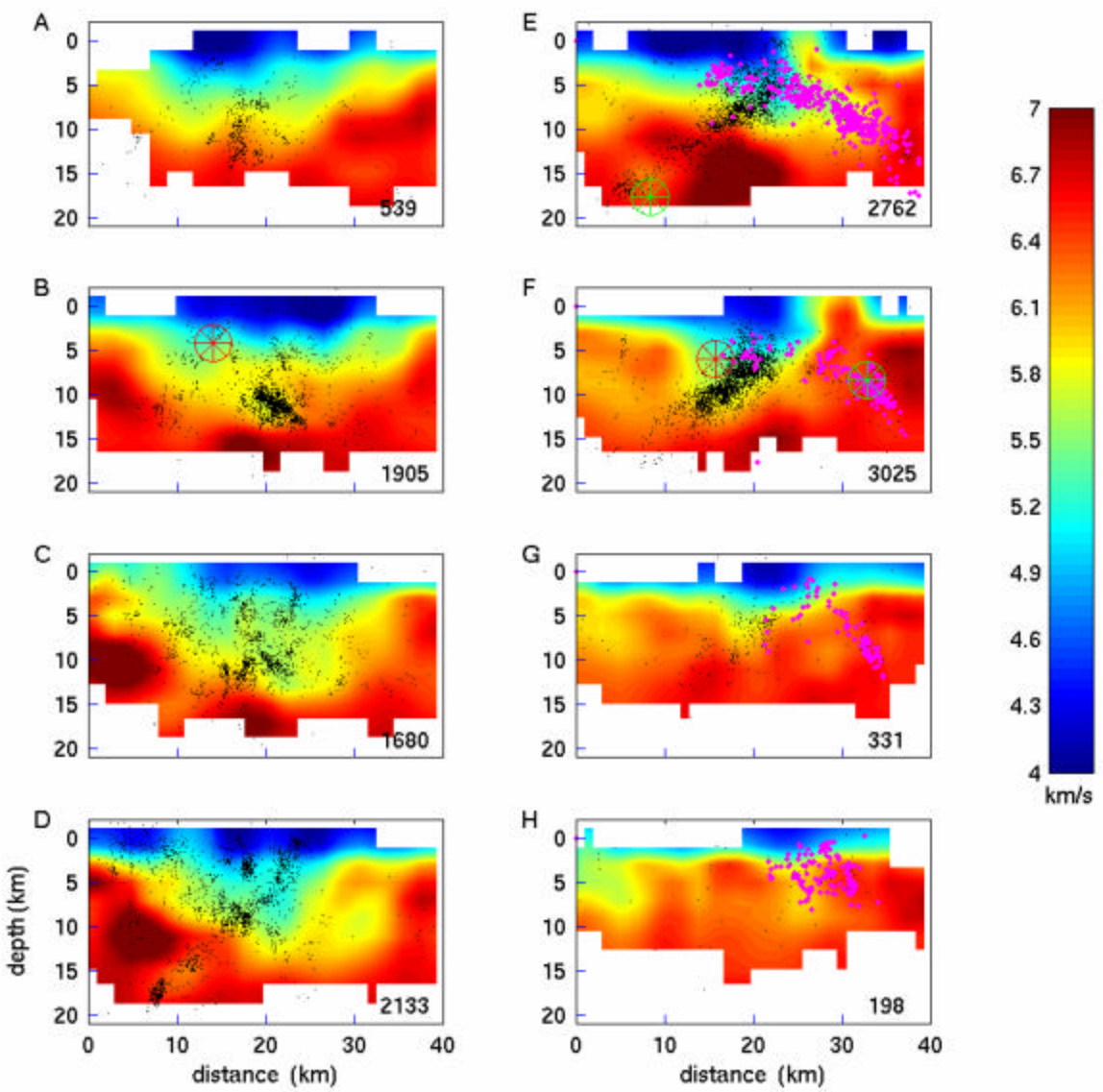
A
B
C
D
E
F
G
H
539
1905
1680
2133
2762
3025
331
198
depth (km)
distance (km)
distance (km)
km/s
7
6.7
6.4
6.1
5.8
5.5
5.2
4.9
4.6
4.3
4

Figure 2

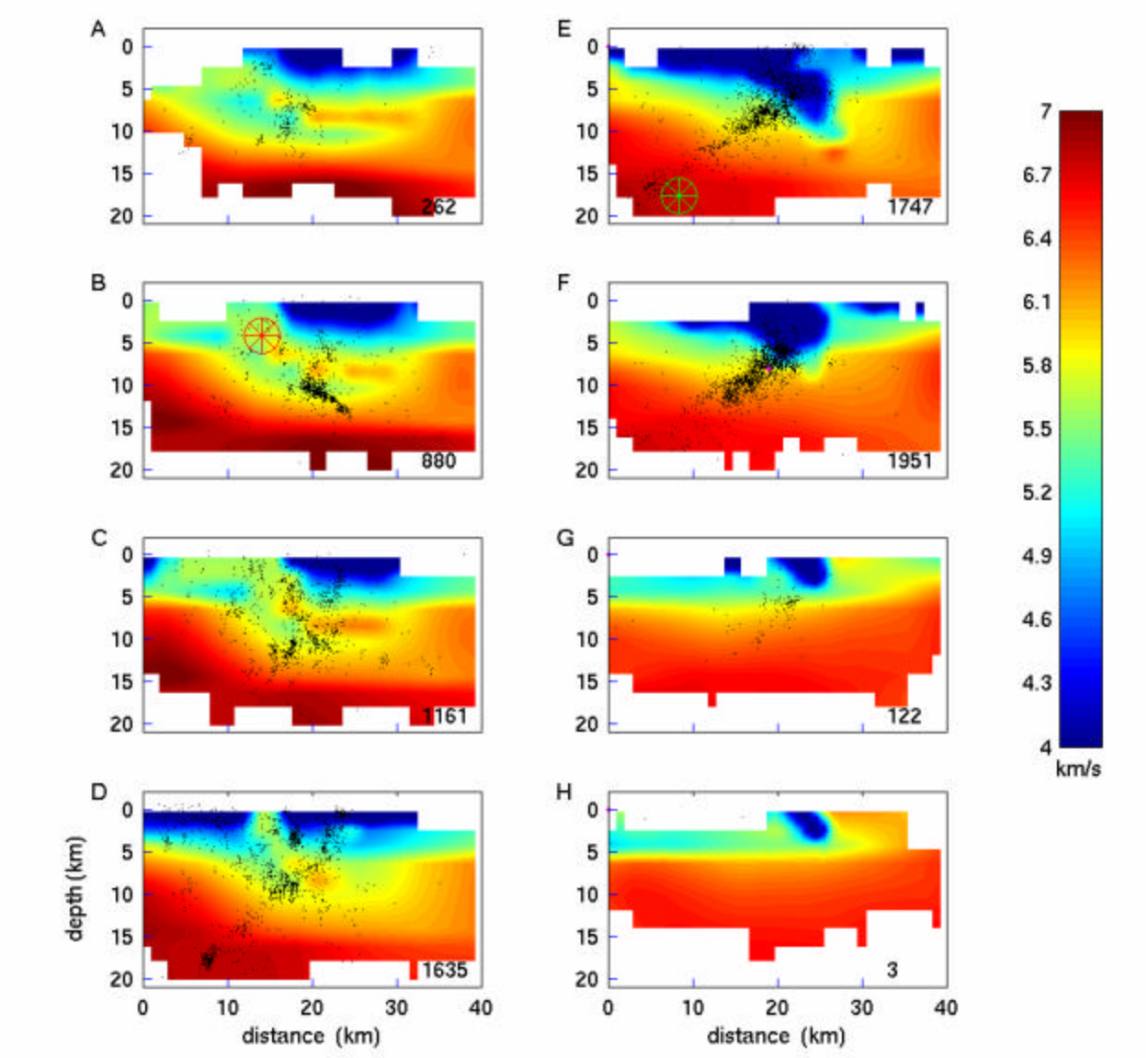
A
B
C
D
E
F
G
H
262
880
1161
1635
1747
1951
122
3
depth (km)
distance (km)
distance (km)
km/s
7
6.7
6.4
6.1
5.8
5.5
5.2
4.9
4.6
4.3
4

Figure 3

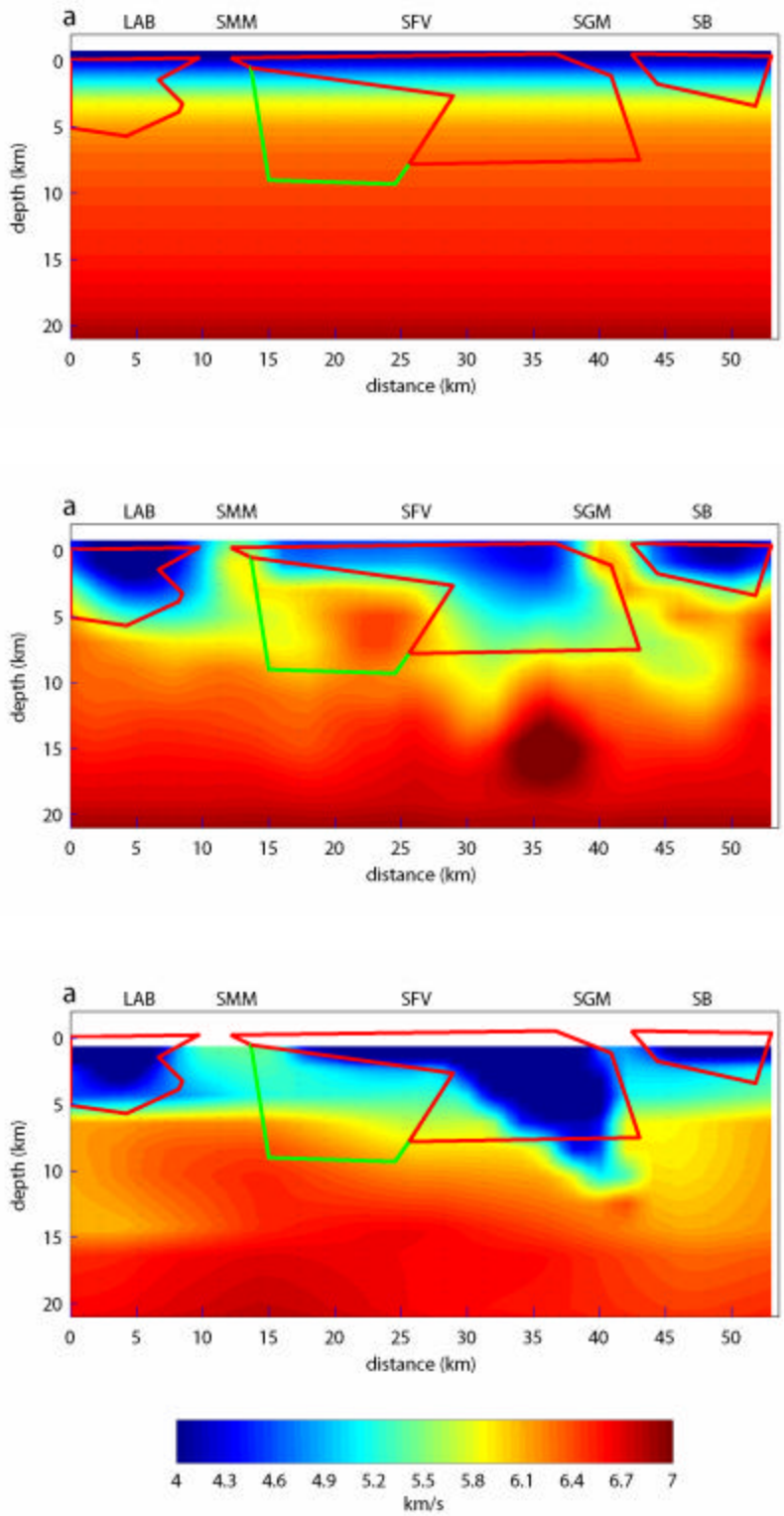
a
LAB
SMM
SFV
SGM
SB
depth (km)
distance (km)
0
5
10
15
20
25
30
35
40
45
50
4
4.3
4.6
4.9
5.2
5.5
5.8
6.1
6.4
6.7
7
km/s

Figure 4

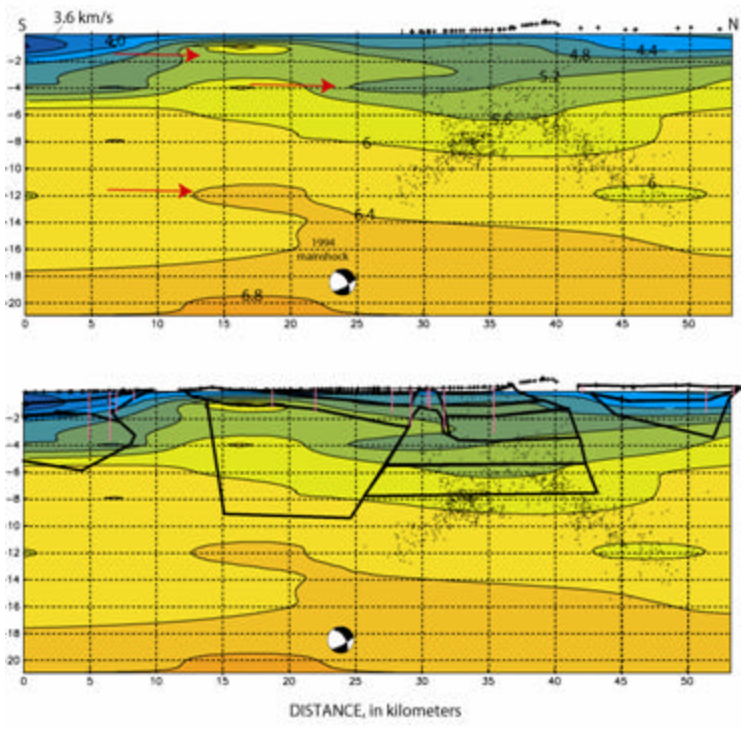

Figure 5

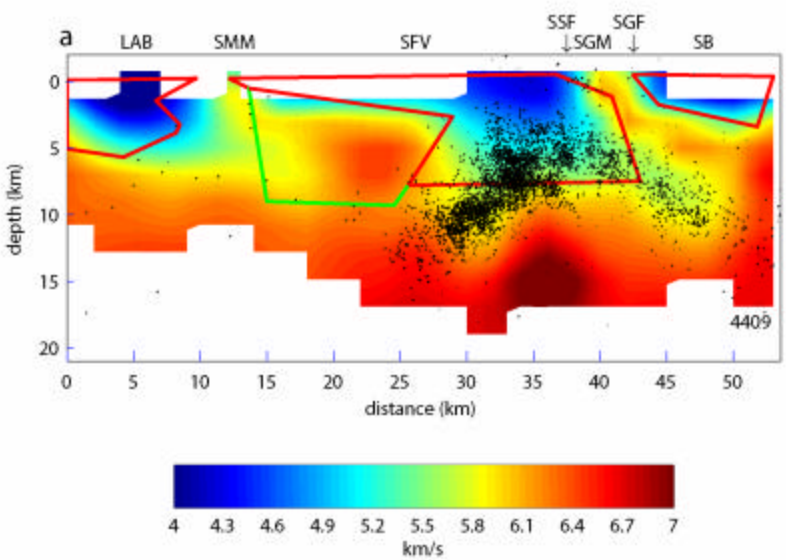

Figure 6

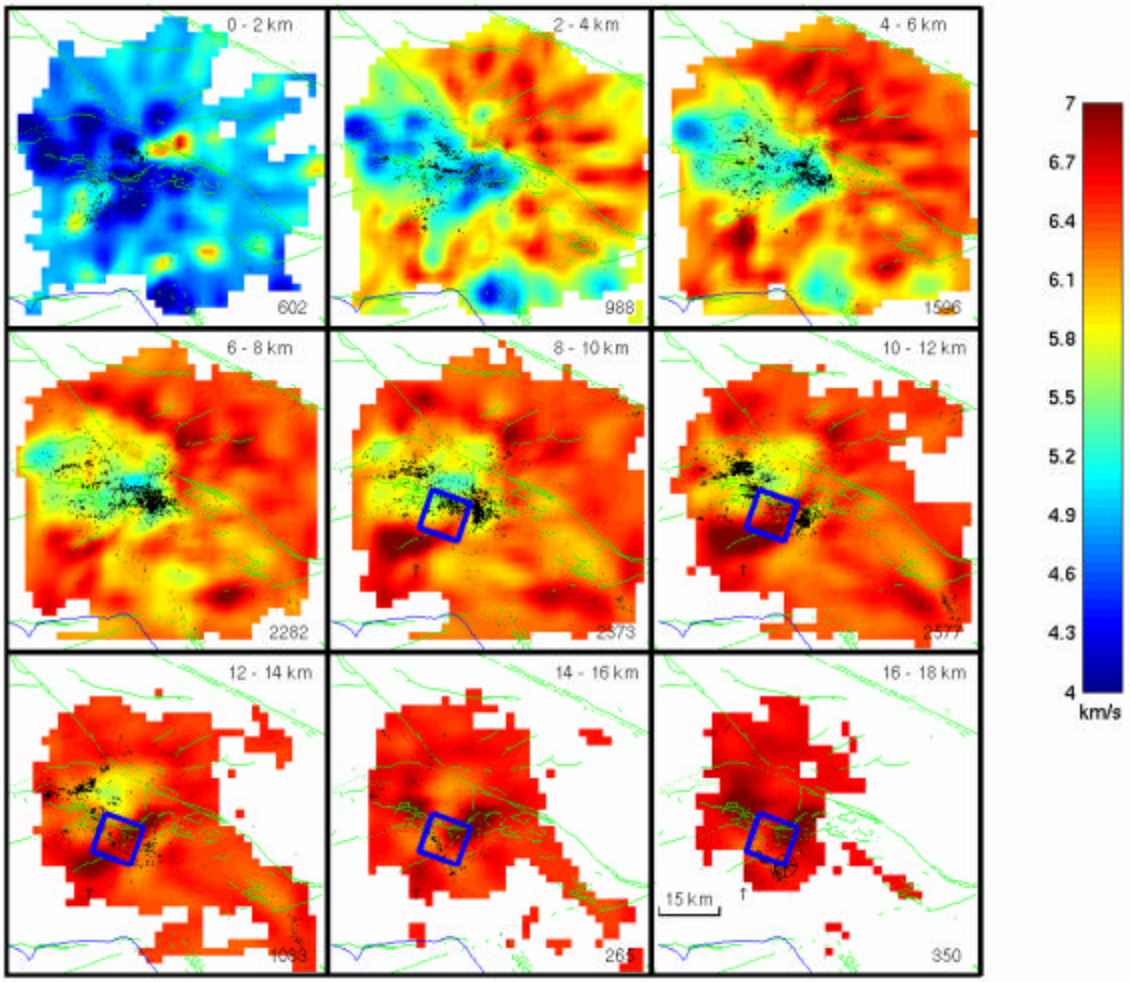
0 - 2 km
602
2 - 4 km
988
4 - 6 km
1596
6 - 8 km
2282
8 - 10 km
2573
10 - 12 km
12 - 14 km
14 - 16 km
16 - 18 km
15 km
350
7
6.7
6.4
6.1
5.8
5.5
5.2
4.9
4.6
4.3
4
km/s

Figure 7

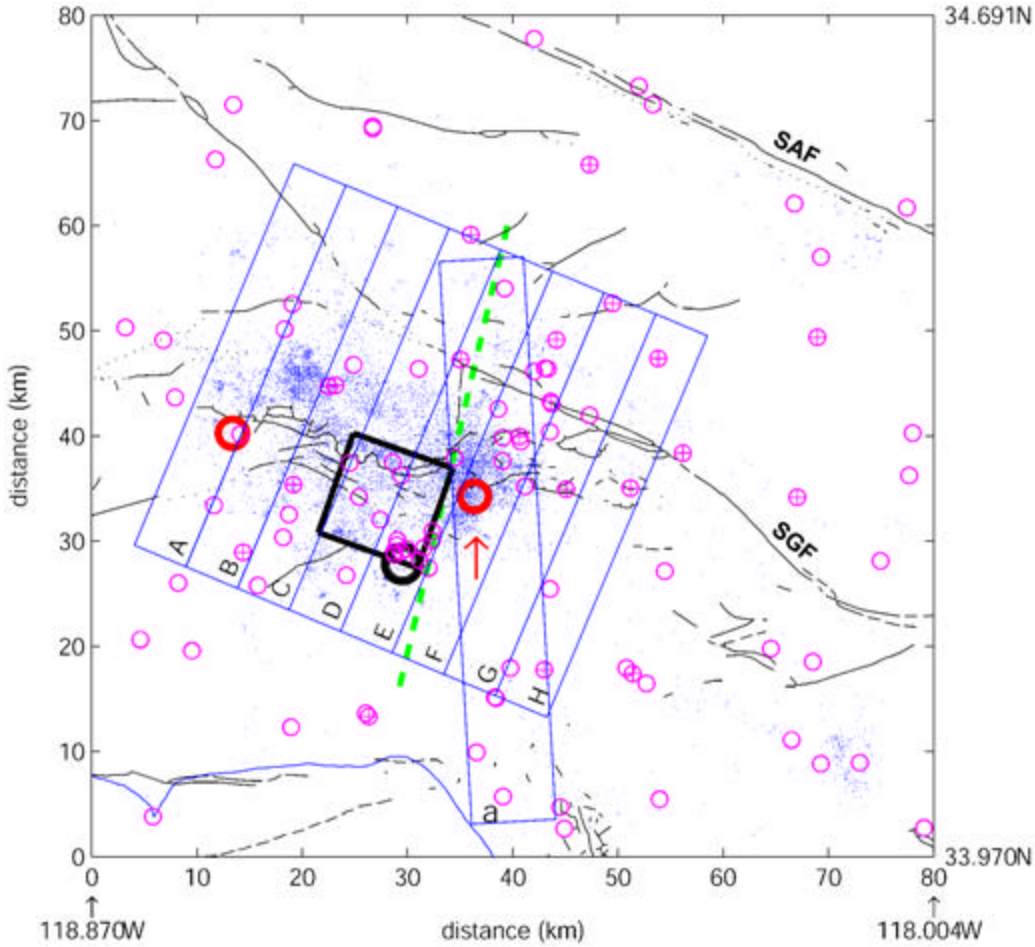
34.691N
33.970N
118.870W
118.004W
distance (km)
distance (km)
SAF
SGF
A
B
C
D
E
F
G
H
a
b
0
10
20
30
40
50
60
70
80

Figure 8

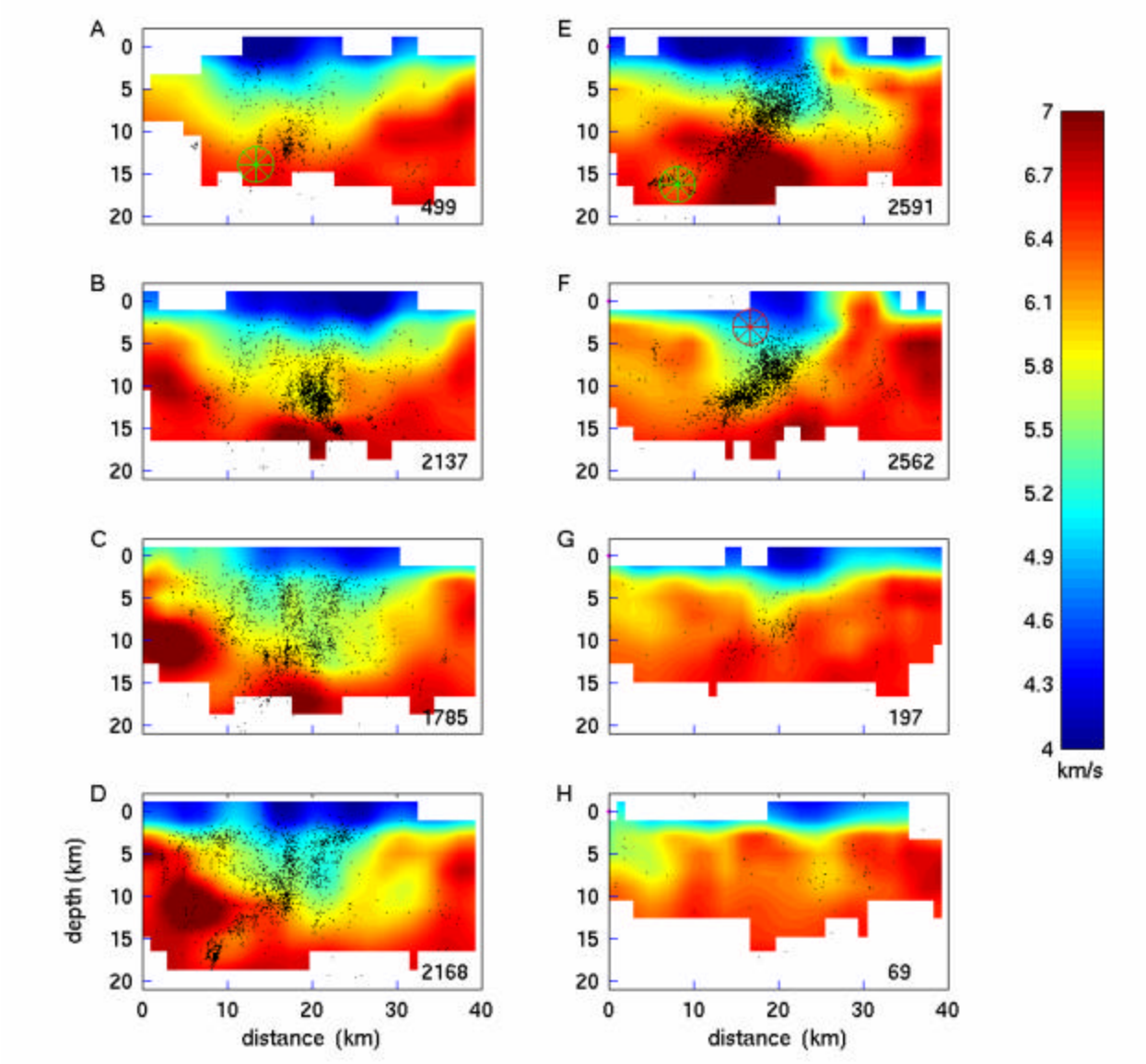
A
B
C
D
E
F
G
H
499
2591
2137
2562
1785
197
2168
69
depth (km)
distance (km)
distance (km)
km/s
7
6.7
6.4
6.1
5.8
5.5
5.2
4.9
4.6
4.3
4

Figure 9

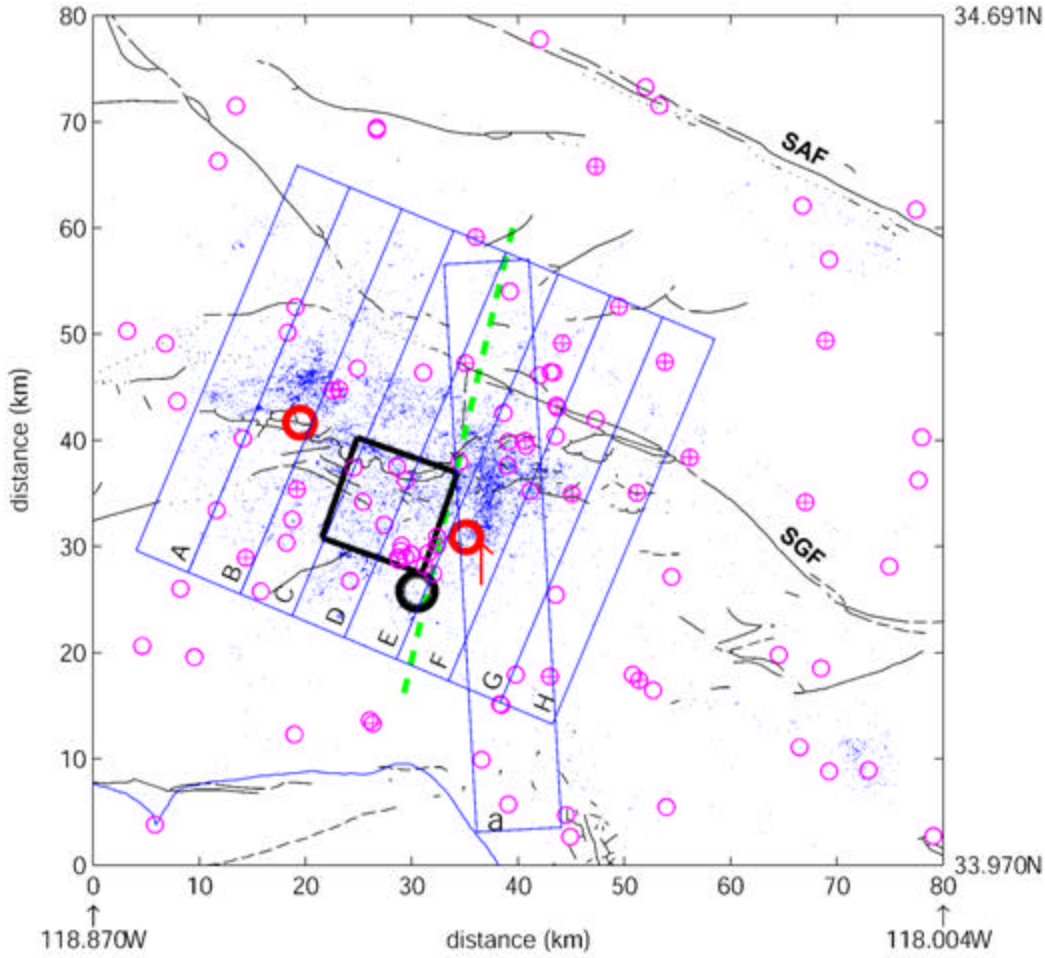
34.691N
33.970N
118.870W
118.004W
distance (km)
distance (km)
SAF
SGF
A
B
C
D
E
F
G
H
a
0
10
20
30
40
50
60
70
80

Figure 10

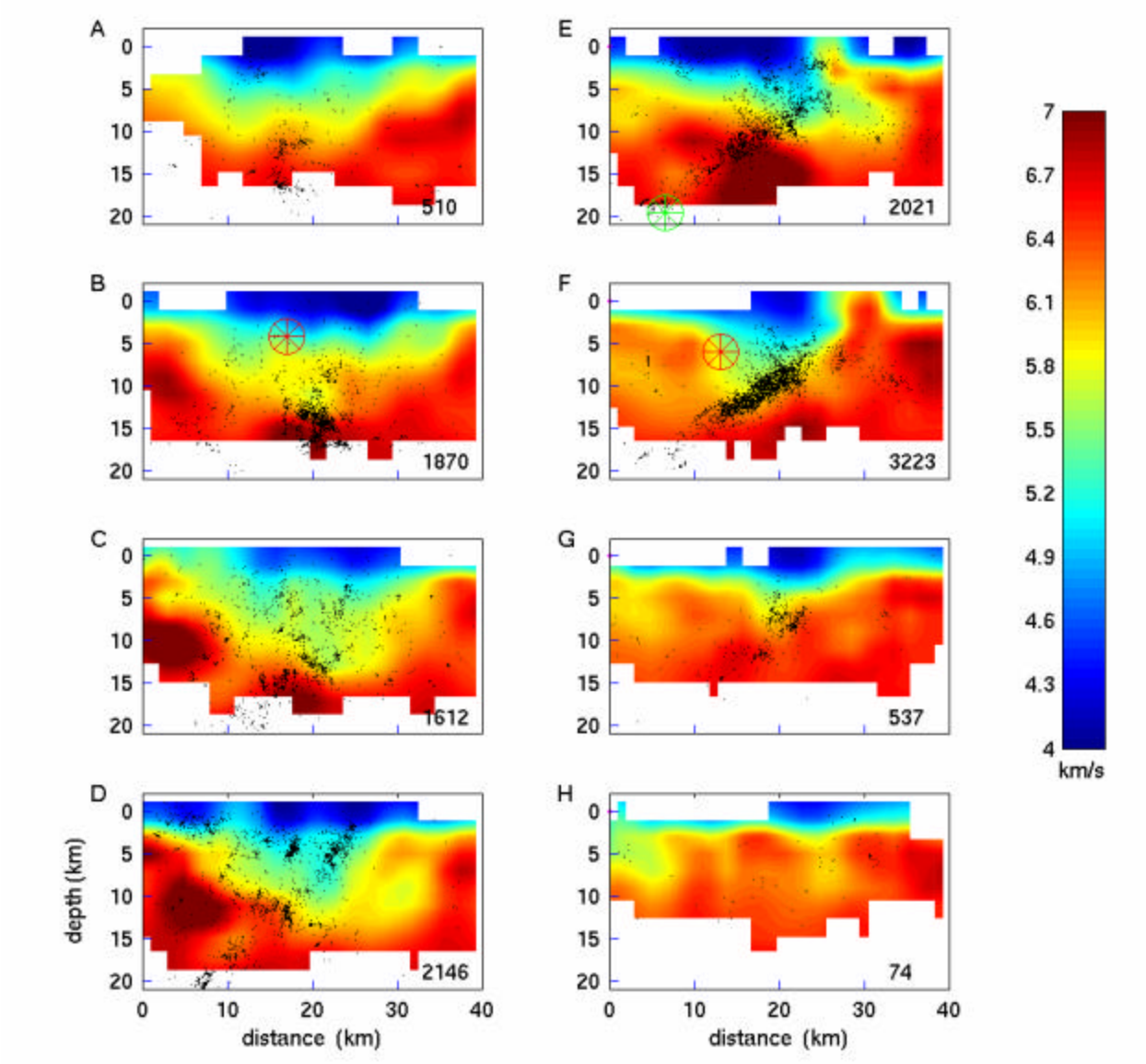
A
B
C
D
E
F
G
H
510
1870
1612
2146
2021
3223
537
74
depth (km)
distance (km)
km/s
7
6.7
6.4
6.1
5.8
5.5
5.2
4.9
4.6
4.3
4

Figure 11